Electronic Supplementary Information

Interplay between coordination sphere engineering

and properties of nickel diketonate-diamine complexes

as vapor phase precursors for the growth of NiO thin films

Mattia Benedet,[a] Davide Barreca,*[b] Ettore Fois,[c] Roberta Seraglia,[b] Gloria Tabacchi,*[c]

Marco Roverso,[a,b] Gioele Pagot,[d] Cristiano Invernizzi,[c] Alberto Gasparotto,[a,b]

Alexandra A. Heidecker,[e] Alexander Pöthig,[e] Emanuela Callone,[f] Sandra Dirè,[f]

Sara Bogialli,[a,b] Vito Di Noto[d] and Chiara Maccato[a,b]

[a.] *Department of Chemical Sciences -Padova University and INSTM, Via Marzolo 1, 35131 Padova, Italy*

[b.] *CNR-ICMATE and INSTM - Department of Chemical Sciences - Padova University, Via Marzolo 1, 35131 Padova, and Corso Stati Uniti 4, 35127 Padova, Italy.*

[c.] *Department of Science and High Technology - Insubria University and INSTM, Via Valleggio 11, 22100 Como, Italy.*

[d.] *Section of Chemistry for the Technology (ChemTech), Department of Industrial Engineering – Padova University and INSTM, Via Marzolo 9, 35131 Padova, Italy*

[e.] *Catalysis Research Center & Department of Chemistry - Technische Universität München, Lichtenbergstr. 4, 85747 Garching, Germany*

[f.] *"Klaus Müller" Magnetic Resonance Laboratory, Department of Industrial Engineering - Trento University, Via Sommarive 9, 38123 Trento, Italy*

* Authors to whom correspondence should be addressed; e-mail: davide.barreca@unipd.it ; (D.B.); gloria.tabacchi@uninsubria.it (G.T.).

Table of Contents

§ S1. Crystallization attempts for [Ni(fod)$_2$TMEDA] (2)

Crystallization technique	Solvent	Temperature (°C)	Digital photograph
Solvent evaporation	CH$_3$CH$_2$OH	20	
		4	
		-18	
Solvent evaporation	CHCl$_3$	20	
		4	
		-18	
Solvent evaporation	CH$_2$Cl$_2$	20	
		4	
		-18	
Liquid diffusion	CH$_2$Cl$_2$, CH$_3$CN and (CH$_3$CH$_2$)$_2$O	20	
Vapor diffusion	CH$_3$CN, CH$_2$Cl$_2$, (CH$_3$CH$_2$)$_2$O and CH$_3$CH$_2$OH	20	

Table S1 Summary of the main crystallization attempts carried out for [Ni(fod)$_2$TMEDA] (**2**).

§ S2. Structural characterization

§ S2.1 Experimental

For [Ni(tfa)$_2$TMEDA] (**1**) and [Ni(thd)$_2$TMEDA] (**3**), a total of 3970 and 4231 frames were collected. The corresponding total exposure times were 3.11 and 5.48 h, respectively. Measurements were performed on a single crystal coated with perfluorinated ether fixed on the top of a Kapton micro sampler, transferred to the diffractometer and frozen under a cold nitrogen stream. A matrix scan was used to determine the initial lattice parameters. The reflections were merged and corrected for Lorentz and polarization effects, scan speed and background with the Bruker SAINT[1] software package using a narrow-frame algorithm. Absorption correction, including odd and even-ordered spherical harmonics, was carried out using SADABS.[2] The space group was assigned based on systematic absences, E-statistics and structure refinement. The structures were solved using direct methods with aid of successive difference Fourier maps, and refined using APEX4 software, in conjugation with SHELXL-2019/1 and SHELXLE.[3-5] Hydrogen atoms were calculated in ideal positions with $U_{iso}(H) = 1.2\ U_{eq}(C)$ and non-hydrogen atoms were refined using anisotropic displacement parameters. Full-matrix least-squares refinements were performed through the minimization of $[\Sigma w(F_o^2 - F_c^2)^2]$ with the SHELXL weighting scheme.[3] Neutral atom scattering factors and anomalous dispersion corrections for non-hydrogen atoms were taken from International Tables for Crystallography.[6] A split layer refinement was adopted for disordered groups using additional restraints on geometries and anisotropic displacement parameters. MERCURY[7] was used to generate images of the crystal structure.

Supplementary crystallographic data for this paper are contained in CCDC 2245881 {[Ni(tfa)$_2$TMEDA], (**1**)} and 2245880 {[Ni(thd)$_2$TMEDA], (**3**)}. These data are provided free of charge by the Cambridge Crystallographic Data Centre.

	[Ni(tfa)$_2$TMEDA] (1)	[Ni(thd)$_2$TMEDA] (3)
Empirical formula	C$_{16}$H$_{24}$O$_4$N$_2$F$_6$Ni	C$_{28}$H$_{54}$O$_4$N$_2$Ni
M_r	481.06	541.43
T (K)	100(2)	100(2)
Crystal size (mm^3)	0.194×0.279×0.461	0.312×0.353×0.531
Crystal habit	clear light green fragment	clear light blue fragment
Crystal system	monoclinic	monoclinic
Space group	$P\,2_1/c$	$P\,2_1/n$
a (Å)	8.1172(5)	9.9651(7)
b (Å)	20.0104(11)	18.8124(15)
c (Å)	12.6925(8)	17.0424(13)
α (°)	90	90
β (°)	91.113(2)	93.966(3)
γ (°)	90	90
V (Å^3)	2061.2(2)	3187.2(4)
Z	4	4
ρ_{calc} (g×cm^{-3})	1.550	1.128
μ (mm^{-1})	1.018	0.639
F(000)	992	1184
θ range	1.90-27.48	2.17-26.02
Reflections collected	136697	124158
Independent reflections	4736	6273
R_{int}	0.0503	0.0304
Coverage independent reflections (%)	99.9	99.9
Absorption correction	Multi-scan	Multi-scan
Max., min transmission	0.6873, 0.7457	0.8250, 0.7280
Observed data [$I > 2\sigma(I)$]	4595	6016
Parameters/restraints	326/181	391/499
Goodness-of-fit on F^2	1.167	1.036
Δ/σ_{max}	0.002	0.001
R_1 [$I > 2\sigma(I)$]	0.0296	0.0411
wR2 [$I > 2\sigma(I)$]	0.0701	0.1062
R_1 (all data)	0.0304	0.0423
wR_2 (all data)	0.0705	0.1073
Residuals (e×Å^{-3})	0.493/-0.591	0.746/-0.536
R.M.S. deviation from mean / eÅ^{-3}	0.060	0.060

Table S2 Crystallographic data and refinement details for compounds **1** and **3**.

§ S2.2 Comment on the previously reported [Ni(tfa)$_2$TMEDA] (1) structure (CCDC 2099619)
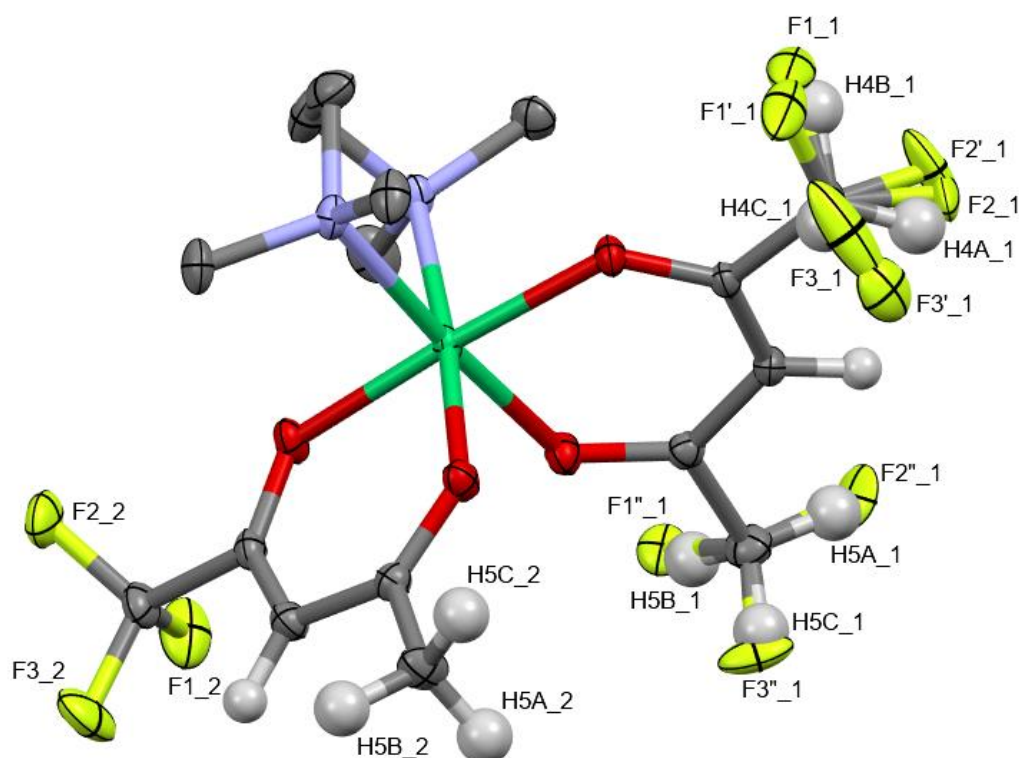
Fig. S1 Previously reported model of the solid-state molecular structure of **1** (CCDC 2099619).[8] Selected hydrogen atoms are omitted for clarity and ellipsoids are depicted at 50% probability level. The used labelling is in accordance with the reported cif file.

In general, the model shows a disorder similar to the one determined in the measurements. Nevertheless, we detected a minor error in the split layer refinement instructions of the model, which resulted in slight deviations of the ratio between the isomers, as briefly explained in the following.

To refine the positional disorder, three layers had to be modeled (two for the CF$_3$ group orientation, and an additional one for the rotational disorder in one orientation). Therefore, the SUMP card was used in SHELXL. The following SUMP commands were applied:

SUMP 1 0 1 2 1 3 1 6
SUMP 1 0 1 4 1 5

leading to the corresponding free variables:

FVAR	0.14227	0.47333	0.47652	0.03521	0.96479	0.05015
	(FVAR1)	**(FVAR2)**	**(FVAR3)**	**(FVAR4)**	**(FVAR5)**	**(FVAR6)**

and the corresponding parts using the defined free variables:

PART 1 21 **(FVAR 2)**
C4   1   0.433492   0.385576   0.242266   21.00000   0.02475   0.01342 =

0.03538 -0.00718 -0.00602   0.00473

F1   3   0.591796   0.400590   0.205243   21.00000   0.01486   0.02479 =
    0.11100 -0.01266   0.00541   0.00404

F2   3   0.387576   0.340347   0.168423   21.00000   0.02660   0.01407 =
    0.05250 -0.01637 -0.00622   0.00274

F3   3   0.444394   0.360524   0.328831   21.00000   0.14468   0.04237 =
    0.01952   0.00561   0.00122   0.05827

PART 2 31   (FVAR 3)

C4' 1   0.433492   0.385576   0.242266   31.00000   0.02475   0.01342 =
    0.03538 -0.00718 -0.00602   0.00473

F1' 3   0.583349   0.392192   0.277722   31.00000   0.01881   0.01883 =
    0.12301 -0.00588 -0.01291   0.00553

F2' 3   0.418607   0.346236   0.163354   31.00000   0.08916   0.02686 =
    0.01762 -0.00368   0.00762   0.02720

F3' 3   0.362621   0.347002   0.326432   31.00000   0.04962   0.02360 =
    0.02913   0.01097   0.00213   0.00898

PART 3 41   (FVAR 4)

C4" 1   0.433492   0.385576   0.242266   41.00000   0.02475   0.01342 =
    0.03538 -0.00718 -0.00602   0.00473

AFIX 33

H4A 2   0.371591   0.349831   0.206621   41.00000 -1.50000
H4B 2   0.540067   0.391409   0.208285   41.00000 -1.50000
H4C 2   0.451641   0.373780   0.316650   41.00000 -1.50000

AFIX   0
PART 0

PART 4 51   (FVAR 5)

C5   1 -0.092610   0.491977   0.123908   51.00000   0.01815   0.02745 =
    0.02432 -0.00148 -0.00305 -0.00144

AFIX 137

H5A 2 -0.086024   0.454367   0.074706   51.00000 -1.50000
H5B 2 -0.126904   0.532196   0.085333   51.00000 -1.50000
H5C 2 -0.173261   0.481873   0.178277   51.00000 -1.50000

AFIX   0

PART 5 61   (FVAR 6)

C5' 1 -0.092610   0.491977   0.123908   61.00000   0.01815   0.02745 =
    0.02432 -0.00148 -0.00305 -0.00144

F1" 3 -0.119915   0.549909   0.071622   61.00000   0.02124   0.02729 =
    0.02248   0.00427 -0.01131   0.00274

F2" 3 -0.080076 0.445526 0.053502 61.00000 0.03252 0.03170 =
0.02387 -0.00558 -0.01720 -0.01053
F3" 3 -0.194571 0.483606 0.194344 61.00000 0.01249 0.05838 =
0.02692 0.01735 -0.00217 -0.00346
PART 0

Hereby, PART 1-3 are the individual split layers of one carbon atom C4 (2 rotation layers of CF_3, 1 layer of CH_3) and PART 4 and 5 are the two possible orientation layers of C5 (CF_3 vs. CH_3) without an additional rotation. Therefore, PART 1-3 should add up to 1 (= FVAR2 + FVAR3 + FVAR4) as the occupation factor for all C4 layers. Likewise, PART 4+5 should also add up to 1 (= FVAR5 + FVAR6) as the occupation factor for all C5 layers. Nevertheless, using the above-mentioned SUMP card, it was defined that FVAR2 + FVAR3 + FVAR6 ("*SUMP 1 0 1 2 1 3 1 6*") should add up to 1 as well as FVAR4 + FVAR5 ("*SUMP 1 0 1 4 1 5*") add up to 1. As a consequence, the resulting combined occupation factor of all layers of C4 (=C4 + C4' + C4'') is only 0.985 (= FVAR2 + FVAR3 + FVAR4, if correctly added all parts of C4), whereas the combined occupancy factor of all layers C5 (=C5 + C5') amounts to 1.015. Of course, both have no physical sense. The correct command should be:

SUMP 1 0 1 2 1 3 1 4
SUMP 1 0 1 5 1 6

leading to a following slightly different set of free variables:

FVAR 0.14227 0.47257 0.47594 0.05149 0.94979 0.05021

§ S3. Computational analysis

The geometry optimizations of the complexes, considered as isolated molecules, was performed in the framework of hybrid DFT with Gaussian basis set and spin multiplicity = 3. In particular, the optimized structures were calculated with Gaussian 09[9] using the hybrid functional ωB97XD,[10] employing the D95V(d) basis set for H, C, N, O, F atoms.[11] Ni was described via a pseudopotential (SDD ecp).[12] Where available, the starting coordinates for the geometry optimization procedure were taken from crystallographic data. Significant geometrical parameters of the resulting minimum energy structures are reported in Table 1 of the main paper. Despite DFT structural parameters refer to isolated complexes, data in Table 1 indicate that computed bond lengths and angles are in good agreement with experimental ones. This observation highlights the reliability of compound **2** molecular structure, obtained solely by modelling, providing thus a firm ground for a comparative discussion on the structural characteristics of the three target Ni(II) complexes.

In the case of **1**, three possible structures, characterized by the different relative positioning of $-CF_3$ groups, were evaluated (Fig. S2). The first one (Fig. S2A) corresponds to the main component detected in the X-ray diffraction measurements of **1** (isomer **1b**) and exhibits both $-CH_3$ groups in *trans* position with respect to the diamine ligand. According to DFT results, the geometry shown in Fig. S2A represents the minimum energy structure of **1** (also reported in Fig. 1C). As discussed in the main paper text, the crystallographic data for isomer **1b** indicated an additional disorder, ascribed to the rotation of the $-CF_3$ groups. For this reason, we optimized the geometry of the two crystallographic structures of isomer **1b** characterized by different orientations of the $-CF_3$ groups. Importantly, the corresponding geometry optimizations provided a single energy minimum characterized by the $-CF_3$ orientation depicted in Fig. S2A, in line with that exhibited by the main modelled split-layer component.

The optimized structure in Fig. S2B, obtained starting from the crystallographic coordinates of isomer **1a**, is characterized by a $-CH_3$ group and a $-CF_3$ group in the *trans* position with respect to TMEDA. This structure was 0.78 kcal/mol less stable than the minimum energy structure (Fig. S2A). Such a small energy difference may justify the co-presence of both isomers **1b** and **1a** in the crystal structure of **1**. Finally, the optimized geometry shown in Fig. S2C presents both $-CF_3$ groups in *trans* with respect to TMEDA, and was found to be 2.36 kcal/mol less stable than the minimum energy structure (Fig. S2A). This energy difference, appreciably higher than kT, may explain why a structure with both the $-CF_3$ groups in *trans* to TMEDA was not detected experimentally for **1**.

In all the three optimized structures, Ni exhibits a distorted octahedral coordination geometry, where the Ni-O distances in *trans* towards TMEDA are slightly longer than the other Ni-O bonds. Also, in line with the present X-ray data, and previous experimental structural analyses on [Ni(tfa)$_2$TMEDA],[8] Ni-N bond lengths are significantly longer than Ni-O ones.
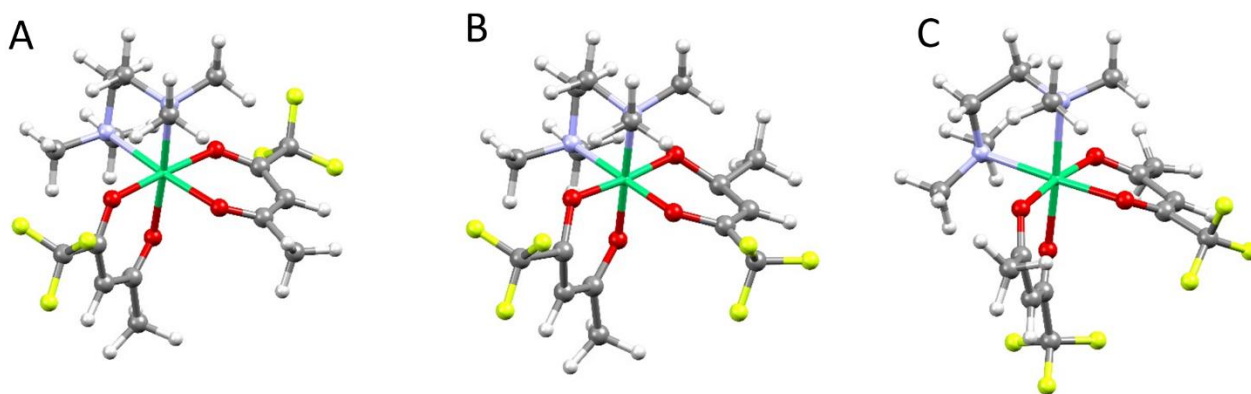
Fig. S2 DFT-calculated optimized geometry of three structural isomers of compound **1**.

At variance from [Ni(tfa)$_2$TMEDA] (**1**) and [Ni(thd)$_2$TMEDA] (**3**), for which single crystal X-ray diffraction data were available, the molecular structure of [Ni(fod)$_2$TMEDA] (**2**) was characterised exclusively on a computational level. For this reason, special attention was devoted to the exploration of the potential energy surface of this system in the search of the minimum energy structure. Specifically, particular care was taken in performing a conformer search involving different orientations of the –CF$_2$-CF$_2$-CF$_3$ chains. The results evidenced that, in spite of the presence of several energy minima spanning an interval of ≈1.5 kcal/mol, the most favourable arrangements of the fluorinated chains are the so-called "ortho" and "staggered" conformations, in line with previous studies.[13] After establishing the most stable arrangements of the –CF$_2$-CF$_2$-CF$_3$ chains, we built up three guess structures for compound **2** by taking the optimized geometries of the three isomers of **1** shown in Fig. S2 and substituting the -CF$_3$ groups with –CF$_2$-CF$_2$-CF$_3$ chains, and the –CH$_3$ groups with *tert*-butyl groups. Geometry optimization provided the three structures reported in Fig. S3, characterized by different positioning of –CF$_2$-CF$_2$-CF$_3$ chains with respect to the TMEDA ligand.

The three optimized geometries of **2** are characterized by a distorted octahedral coordination environment, where Ni-O distances are shorter than Ni-N ones, as for complex **1**. The minimum energy structure (see Fig. S3A and Fig. 1D, main text) has both *tert*-butyl groups in *trans* to TMEDA, while the –CF$_2$-CF$_2$-CF$_3$ chains occupy the apical positions of the Ni coordination sphere. Hence, similar to compound **1**, the positioning of fluorinated groups in *trans* towards the diamine ligand appears to be slightly energetically unfavourable even in **2**. Indeed, the optimized geometry in Fig. S3B presents only one –CF$_2$-CF$_2$-CF$_3$ chain in *trans* to TMEDA, and is 0.91 kcal/mol higher in energy than the minimum energy structure (Fig. S3A). The slight energy difference between these structures may suggest that, as for compound **1**, both isomers might be co-present in solution at room temperature. This finding, along with the presence of possible conformers of **2** characterized by different arrangements of the –CF$_2$-CF$_2$-CF$_3$ chains and very similar energy, might also be one of the reasons of the difficulties encountered in trying to solve the crystal structure of [Ni(fod)$_2$TMEDA] by X-ray diffraction. In a different way, the higher energy difference (2.41 kcal/mol) between the structure shown in Fig. S3C, exhibiting both the –CF$_2$-CF$_2$-CF$_3$ chains in *trans* towards TMEDA, and the minimum energy structure (Fig. S3A), suggests that the co-presence of this isomer might be less likely. This hypothesis is also supported by the fact that, in the case of **1**, no isomer presenting both fluorinated groups in *trans* to TMEDA (see Fig. S2C) was detected by X-ray analyses.
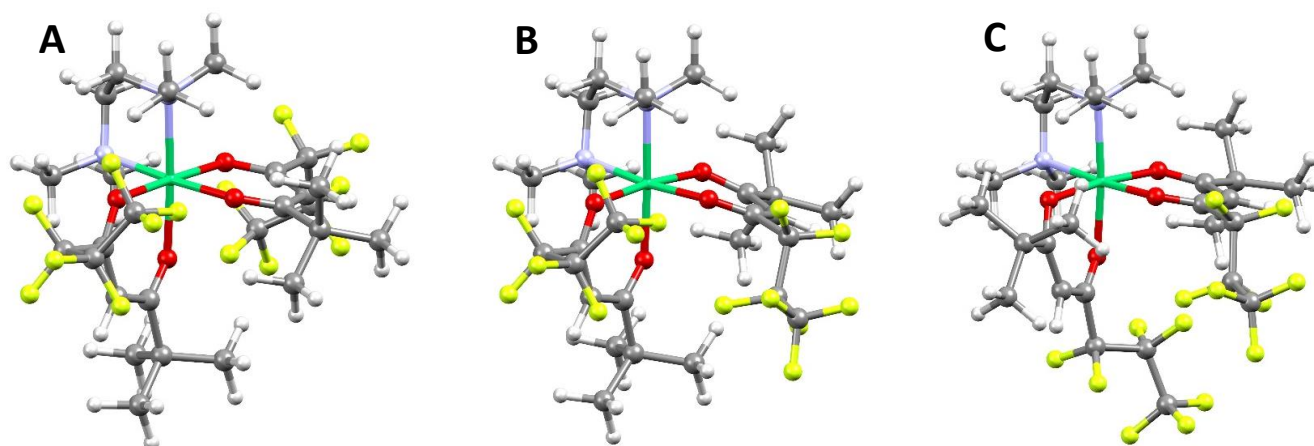
Fig. S3 DFT-calculated optimized geometry of three structural isomers of compound **2**.

XRD data on [Ni(thd)$_2$TMEDA] (**3**) indicated the presence of two isomers characterized by two different TMEDA ethylene bridge arrangements. Starting from the XRD-coordinates of these isomers, two geometry optimizations were performed, which yielded the structures reported in Fig. S4. In the most stable one (Fig. S4A), the ethylene bridge orientation is in line with the one found in the main crystallographic structure component. Conversely, the less stable structure (Fig. S4B), higher in energy by 0.25 kcal/mol, reproduces the TMEDA ethylene bridge arrangement featured in the minor component. This result, in accordance with experimental data, further confirms the reliability of the used theory level in the description of the compound structural features.
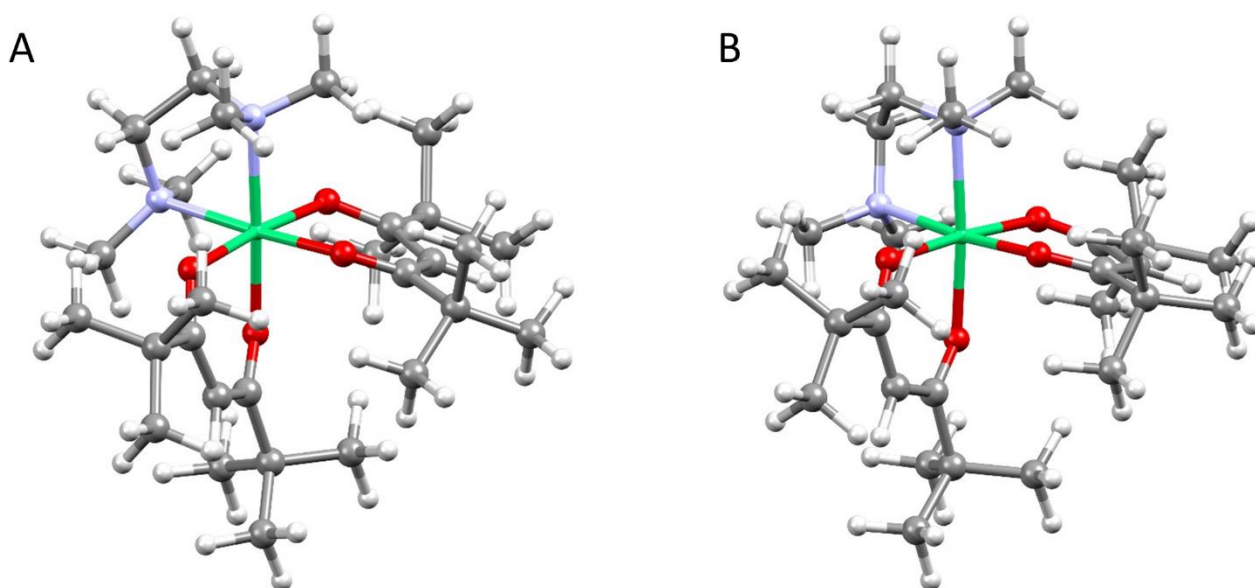
Fig. S4 DFT-calculated optimized geometry of two structural isomers of compound **3**.

§ S4. IR spectroscopy characterization

FTIR analyses were performed with a Thermo Fischer Scientific Nicolet Avatar 330 instrument on KBr pellets (4 cm^{-1} resolution spectra, range 4000–400 cm^{-1}, 64 scans). Experimental IR data were compared with theoretical vibrational frequencies computed on the minimum energy structures of **1-3** (see also § S3), which were characterized by all positive frequencies.

The experimental and simulated IR spectra of [Ni(tfa)$_2$TMEDA], [Ni(fod)$_2$TMEDA], and [Ni(thd)$_2$TMEDA] are displayed in Fig. S5, S6, and S7, respectively. The calculated spectra were broadened with a 2 cm^{-1} gaussian.

For all the compounds, the agreement between experimental and theoretical spectra is satisfactory, allowing thus a detailed band assignment based on the normal modes. Moreover, in the case of [Ni(tfa)$_2$TMEDA], the IR signals and the respective assignments fairly reproduce the ones previously reported for the same complex.[8]

As a general observation, the main spectral features of the three complexes are similar to those of previously reported [M(β-diketonate)$_2$TMEDA] complexes (M = Fe, Mn, Cu, Zn),[14-17] characterized by a similar metal center coordination environment. An interesting trend emerges by comparing the C=O stretching frequencies between the three complexes – namely, the associated wavenumbers are significantly higher for the fluorinated compounds (**1** and **2**) than for the non-fluorinated **3**. This finding is in line with the opposite trend for Ni-O stretching frequencies, which are the highest for **3**, characterized by the strongest Ni-O bonds (see also discussion in the main text).

A detailed assignment of the bands is reported in Tables S3-S5, respectively (wavenumbers refer to computed values; intensities are denoted as vs = very strong; s = strong; m = medium; w = weak; vw = very weak).
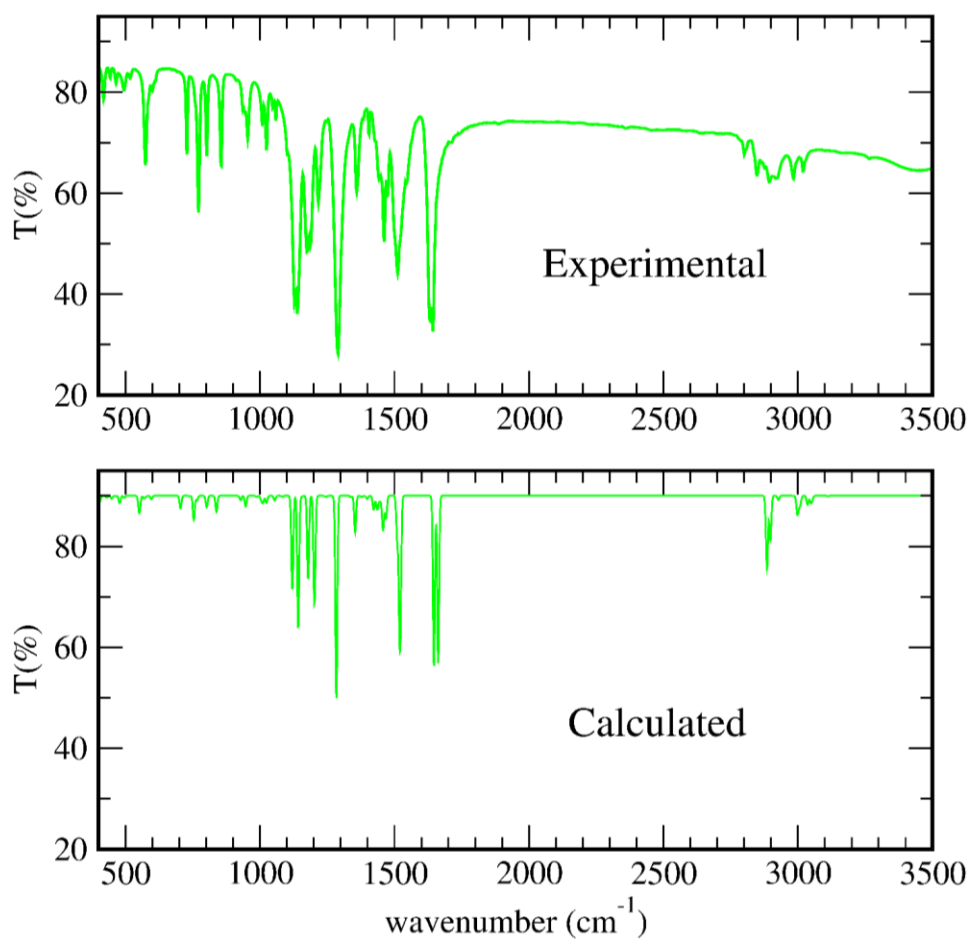
Fig. S5 Experimental and calculated IR spectra of [Ni(tfa)₂TMEDA] (**1**). A scaling factor of 0.952 was applied to the computed vibrational frequencies.[18, 19]

$\tilde{v}$ (cm^{-1})	Assignment
3268 (vw)	Stretching of tfa central C-H
3207-3027 (m,w)	TMEDA –CH$_3$/–CH$_2$ stretching
3188-3075 (m,w)	tfa –CH$_3$/–CH$_2$ stretching
1746 (vs)	Symmetric Stretching C=O in-phase
1730 (vs)	Symmetric Stretching C=O out-of-phase
1599-1586 (vs)	Asymmetric Stretching C=O (involving C=C–C stretching tfa)
1543-1500 (m,w)	Rocking and scissoring of all –CH$_3$/–CH$_2$
1494-1339 (w)	Wagging, rocking, twisting, scissoring of all –CH$_3$/–CH$_2$
1422 (m)	–CH$_3$ tfa scissoring + –CH and C=C–C bending
1349-1347 (vs,s)	TMEDA rocking and scissoring of –CH$_3$/–CH$_2$ +Stretching C–CF$_3$/C=C
1313-1307 (vw)	TMEDA stretching of N-C-C-N
1264-1199 (s)	Stretching C–F + bending –CH tfa + TMEDA –CH$_3$ wagging
1213 (w)	TMEDA -CH$_2$/-CH$_3$ twisting + N-CH$_2$ stretching
1178-1176 (s)	In-plane bending –CH + stretching C-F, C-C=C, C–CF$_3$ tfa
1173-1137 (w)	Twisting –CH$_3$/–CH$_2$ TMEDA + breathing TMEDA
1108 (w)	TMEDA stretching C-C in-phase
1083-1075 (m)	TMEDA collective out-of-plane bending
1055-1037 (w)	In-plane and out-of-plane bending modes tfa (CH-C(=O)-C)
994-974 (w)	Collective bending N-C-C-N TMEDA
880 (m)	Breathing tfa
842-804 (m)	Stretching N-C-C-N TMEDA
791 (m)	Out-of-plane bending O-C-C, C-C-H, -CH$_3$ tfa
578 (m)	Symmetric and asymmetric stretching Ni-O2, Ni-O3
597 (w)	Symmetric out-of-plane bending O2-Ni-O3 (wagging)
503 (m,w)	Symmetric and asymmetric stretching Ni-O1, Ni-O4
471 (m,w)	Symmetric and asymmetric stretching Ni-N1, Ni-N2
424-197 (m,w)	Bending Ni-O, Ni-N bonds (all)
334-276 (w)	Symmetric stretching Ni-O2, Ni-O3
249-216 (w)	Vibration of Ni in out of the O2-O3-N1-N2 plane
228 (w)	Vibration of Ni in the O2-O3-N1-N2 plane
178-16 (w)	Collective stretching/bending modes of the Ni octahedron

Table S3 Calculated wavenumbers $\tilde{v}$ and band assignment for [Ni(tfa)$_2$TMEDA] IR spectra in Fig. S5.
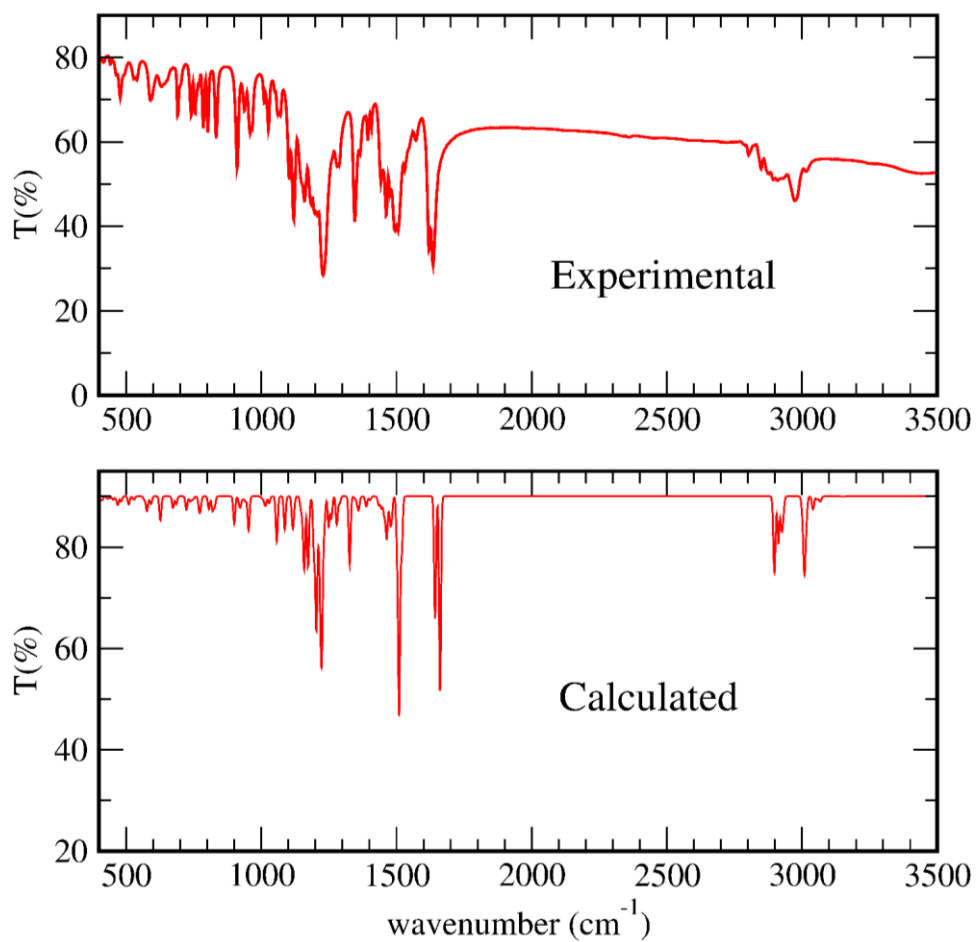
Fig. S6 Experimental and calculated IR spectra of [Ni(fod)₂TMEDA] (**2**). A scaling factor of 0.952 was applied to the computed vibrational frequencies.[18, 19]

$\tilde{\nu}$ (cm^{-1})	Assignment
3298 (wv)	Stretching of fod central C-H
3215-3197 (w)	TMEDA -CH$_3$ asymmetric stretching
3179-3057 (m)	fod -CH$_3$ asymmetric stretching
3156 (m)	TMEDA -CH$_3$ symmetric stretching
3147-3145 (m)	fod and TMEDA -CH$_3$ asymmetric stretching
3044-3027 (m,s)	TMEDA -CH$_3$/-CH$_2$ stretching
3145-3057 (m)	fod -CH$_3$ symmetric stretching
3045 (s)	TMEDA -CH$_2$ stretching
1739 (vs)	Symmetric stretching C=O in-phase
1721 (vs)	Symmetric stretching C=O out-of-phase
1590-1572 (vs)	Asymmetric stretching C=O (involving stretching C=C-C fod)
1552 (m)	fod -CH$_3$ scissoring
1546-1530 (m,s)	TMEDA -CH$_3$/-CH$_2$ wagging, rocking, twisting and scissoring
1523-1466 (m)	TMEDA -CH$_3$/-CH$_2$ in-plane bending
1452-1415 (m)	fod -CH$_3$ in-plane bending
1407 (m)	Rocking TMEDA
1389-1387 (s)	Stretching C=C-C and -CF$_2$-CF$_3$ fod
1349 (m)	TMEDA N-C-C-N wagging and -CH$_3$/-CH$_2$ twisting
1339-1340 (m)	Twisting TMEDA
1337-1306 (m)	Stretching C=C-C-CF$_2$ + fod -CH$_3$ twisting
1315 (m)	Wagging TMEDA
1286-1210 (s)	Collective bending fod
1273 (vs)	Symmetric in-plane bending fod
1271 (m)	TMEDA and fod out-of-plane bending
1266 (s)	Bending C-H fod
1259 (vs)	Bending C-H + Scissoring of -CF$_2$-CF$_2$-CF$_3$ fod
1251-1251(w)	fod -CH$_3$/-CH/-CF$_3$ bending
1238,1212 (w)	Rocking TMEDA
1228,-1210 (s)	Bending C-H + asymmetric stretching –CF$_2$ fod
1200 (m)	fod -CH$_3$/-CH/-CF$_2$/-CF$_3$ in-plane bending
1171-1169 (s)	Stretching C=C-C and -CH$_3$/-CF$_3$ fod wagging
1110 (w)	TMEDA C-C stretching + CH$_3$ wagging
1106 (s)	Breathing fod
1079-1062 (m,w)	Stretching C-N, C-C + bending N-C-C-N TMEDA
999 (s)	Bending modes of fod and TMEDA
996 (m)	Bending C-C=C fod
960 (m)	*tert*-butyl-C stretching + O=C-CF$_2$ stretching
865-806 (m)	fod deformation modes
843 (m)	TMEDA deformation mode
809, 788 (m)	Out-of-plane bending C-H fod
772- 719 (w)	fod breathing modes
618 (w)	Ni-O2, Ni-O3 Symmetric stretching
615 (w)	Ni-O2, Ni-O3 Asymmetric stretching
593-554 (w)	Stretching O1-Ni, O4-Ni, + CF$_2$ deformation modes
533 (vw)	Bending modes of fluorinated chains
532 (w)	Wagging of O-Ni-O and bending modes of fluorinated chains
503-494 (w)	stretching of Ni-ligand bonds (Ni-N1, Ni-N2, Ni-O3, Ni-O2)
490-483 (m,w)	*tert*-butyl bending
472 (w)	Ni-N1, Ni-N2 asymmetric stretching

460, 459 (w)	Stretching Ni-O1, Ni-O4, + deformation $-CF_2$-CF_2-CF_3
451 (vw)	Ni-N symmetric stretching + deformation modes TMEDA
429 (w)	Ni-O symmetric stretching + deformation modes fod
426 (vw)	Ni-O asymmetric stretching
409 (vw)	N1-Ni-N2 stretching + TMEDA twisting
384-285 (w)	TMEDA and fod deformation modes
275 – 13 (vw)	Collective stretching/bending modes of the Ni octahedron

Table S4 Calculated wavenumbers $\tilde{v}$ with band assignment for [Ni(fod)$_2$TMEDA] IR spectra in Fig. S6.
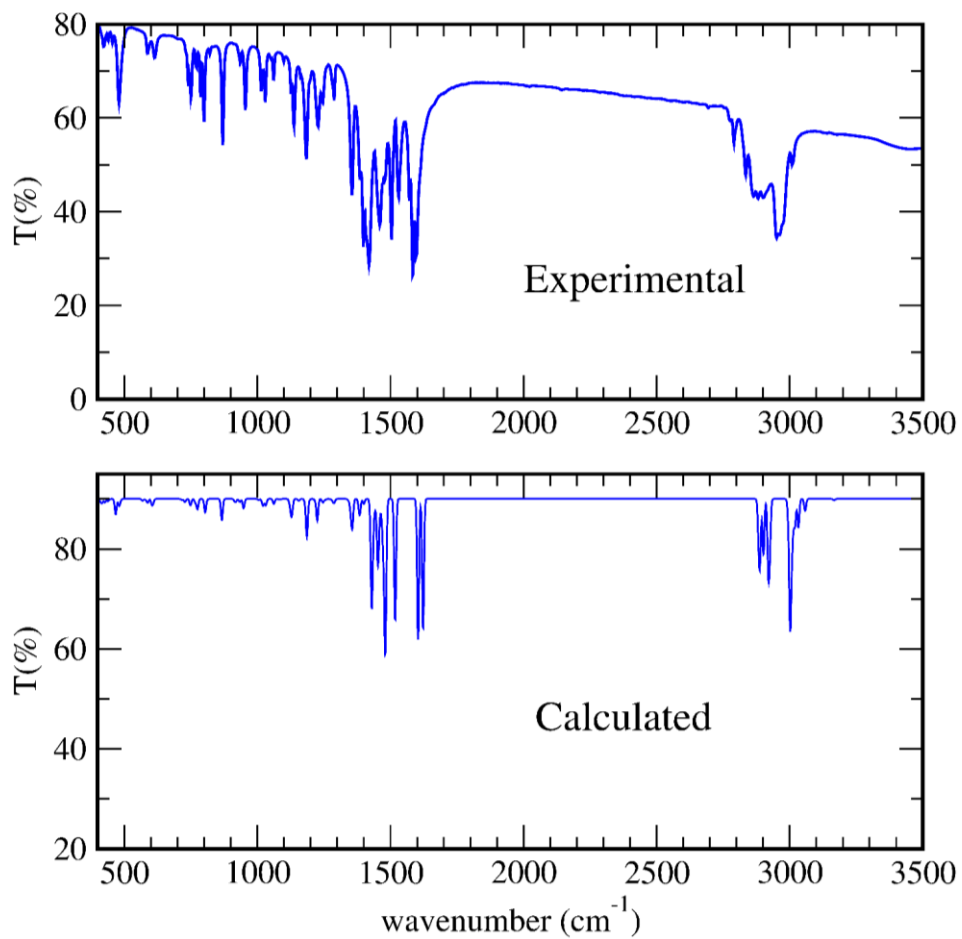
Fig. S7 Experimental and calculated IR spectra of [Ni(thd)₂TMEDA] (**3**). A scaling factor of 0.952 was applied to the computed vibrational frequencies.[18, 19]

$\tilde{v}$ (cm^{-1})	Assignment
3310 (vw)	Symmetric stretching of thd central C-H
3201-3198(m,w)	TMEDA –CH$_3$ stretching
3166-3055(m,w)	Symmetric and asymmetric thd –CH$_3$ stretching
3148-3015(m,w)	thd and TMEDA –CH$_3$ stretching
3146-3015 (m,s)	TMEDA –CH$_3$/-CH$_2$ stretching
3141-3135 (m)	All –CH$_3$ thd stretching
1700 (vs)	Symmetric stretching C=O in-phase
1680 (vs)	Symmetric stretching C=O out-of-phase
1593 (s)	Asymmetric stretching C=O (involving stretching C=C-C thd)
1553 (vs)	Stretching C=C-C thd + collective bending of –CH$_3$ groups
1549 (vs)	Collective rocking and scissoring of –CH$_3$ groups
1547 (w)	All -CH/CH$_2$/-CH$_3$ in-plane-bending + TMEDA -CH$_3$ scissoring
1546-1498 (m)	TMEDA rocking and scissoring of –CH$_3$/–CH$_2$ groups
1533-1500(m,w)	Collective rocking and scissoring of –CH$_3$/–CH$_2$ groups
1508-1495 (m)	Collective rocking /scissoring of –CH$_3$/–CH$_2$ groups + C=C-C thd stretching
1494-1487 (m)	Wagging, rocking, twisting, scissoring of TMEDA –CH$_3$/–CH$_2$
1466-1461 (w)	TMEDA –CH$_2$ wagging + N-CH$_3$ stretching
1450 (w)	thd -C-CH$_3$ collective stretching
1420-1413(m,w)	thd wagging, rocking, twisting, scissoring of C–CH$_3$ *tert*-butyl
1406 (vw)	TMEDA N-C-C-N symmetric out-of-plane-bending
1350 (m,w)	TMEDA N-C-C-N asymmetric out-of-plane-bending
1344 (vw)	thd *tert*-butyl-C-CH$_2$-C-*tert*-butyl symmetric stretching
1310 (vw)	TMEDA stretching N-C-C-N out-of-phase
1282 (m)	thd *tert*-butyl C-CH$_3$ symmetric stretching
1280 (m)	thd *tert*-butyl C-CH$_3$ asymmetric stretching
1246-1244 (s)	O=C-CH-C=O bending
1210 (w)	Collective TMEDA bending
1184 (m)	thd C-CH-C symmetric stretching
1179 (m)	thd C-CH-C asymmetric stretching
1111 (m)	TMEDA stretching C-C in-phase
1080 (m)	TMEDA collective symmetric out-of-plane bending (wagging)
1065 (m)	TMEDA -CH$_2$/-CH$_3$ twisting + N-CH$_2$ stretching
995 (m)	Collective bending N-C-C-N TMEDA
906 (m)	Collective bending thd
840 (m)	Symmetric stretching N-C-C-N
810 (m,w)	Out-of-plane bending O-C-C
804 (w)	TMEDA -CH$_2$ twisting + N-CH$_3$ stretching
779 (m,w)	thd central C-H bending
638,493 (m,w)	Symmetric stretching Ni-O
633, 505 (m)	Asymmetric stretching Ni-O
599,490 (m,w)	Symmetric out-of-plane bending N-Ni-N (wagging)
461 (w)	Asymmetric stretching Ni-N1
447(w)	Symmetric in-plane bending N1-Ni-N2
433-335 (w)	Scissoring and bending O1-Ni-O4
284-256 (m,w)	Bending Ni bonds (all), thd, and TMEDA -CH$_3$
253-22 (vw)	Collective stretching/bending modes of the Ni octahedron

Table S5 Calculated wavenumbers $\tilde{v}$ with band assignment for [Ni(thd)$_2$TMEDA] IR spectra in Fig. S7.

§ S5. NMR spectroscopy characterization

$[Ni(tfa)_2TMEDA]$ **(1)**

$[Ni(fod)_2TMEDA]$ **(2)**

$[Ni(thd)_2TMEDA]$ **(3)**

Fig. S8 ^{1}H-NMR spectra of compounds **1**-**3** in CDCl$_3$.

Fig. S8 displays ^{1}H-NMR spectra of the three complexes. As in the case of ^{13}C, the presence of Ni deteriorates even the quality of ^{1}H spectra. Based on the peak intensities and the results of selective irradiation, as well as on previous works on similar compounds,[20, 21] it is possible to suggest the assignment presented in Table S6. The spectrum of [Ni(tfa)$_2$TMEDA] (**1**) produces a lower resolution with respect to similar compounds with different metal centres.[20, 21] In addition, it is worth mentioning that, as reported, the most sensitive protons lay on the equatorial N-Ni-N axis, thus experiencing a large downfield shift.[22, 23] Furthermore, the induced down- or up-field shift is related to the distance in terms of even/odd bond number.[24] Accordingly, CH$_2$ groups from the tfa ligand shift upfield to -10.7 ppm, whereas methyl protons remain in the 1-6 ppm region with only slight shifts. TMEDA proton resonances are broadened and downfield-shifted in the 100-40 ppm range. Similarly, as concerns [Ni(thd)$_2$TMEDA] (**3**), TMEDA CH$_3$ and CH$_2$ groups downfield shift in the 90-50 ppm region (16H), methyl protons of the two thd units experience only a slight downfield shift to 4.6 ppm (36H) due to the distance from Ni center, whereas the two methylene protons fall at 1 and -13 ppm. [Ni(fod)$_2$TMEDA] (**2**) presents various similarities with [Ni(thd)$_2$TMEDA] and, accordingly, analogous considerations hold for the pertaining NMR spectrum. The effect of fluorinated chains is indirectly visible in the different chemical shifts.

	δ (ppm)	assignment	ligand
[Ni(tfa)$_2$TMEDA] (1)	97.1	CH$_3$	TMEDA
	90.5	CH$_2$	TMEDA
	74.9	CH$_3$	TMEDA
	43.5	CH$_2$	TMEDA
	5.8–1.8	CH$_3$	tfa
	-10.7	CH$_2$	tfa
[Ni(fod)$_2$TMEDA] (2)	96.1	CH$_3$	TMEDA
	87.9	CH$_2$	TMEDA
	73.6	CH$_3$	TMEDA
	47.2	CH$_2$	TMEDA
	4.7	CH$_3$	fod
	3.8 to -1	CH$_2$	fod
	-11	CH$_2$	fod
[Ni(thd)$_2$TMEDA] (3)	83.6	CH$_3$	TMEDA
	76.8	CH$_2$	TMEDA
	61.8	CH$_3$	TMEDA
	56.1	CH$_2$	TMEDA
	4.6	CH$_3$	thd
	1.1	CH$_2$	thd
	-13.5	CH$_2$	thd

Table S6 Chemical shifts and assignments of the resonances in the ^{1}H spectra of Fig. S8.
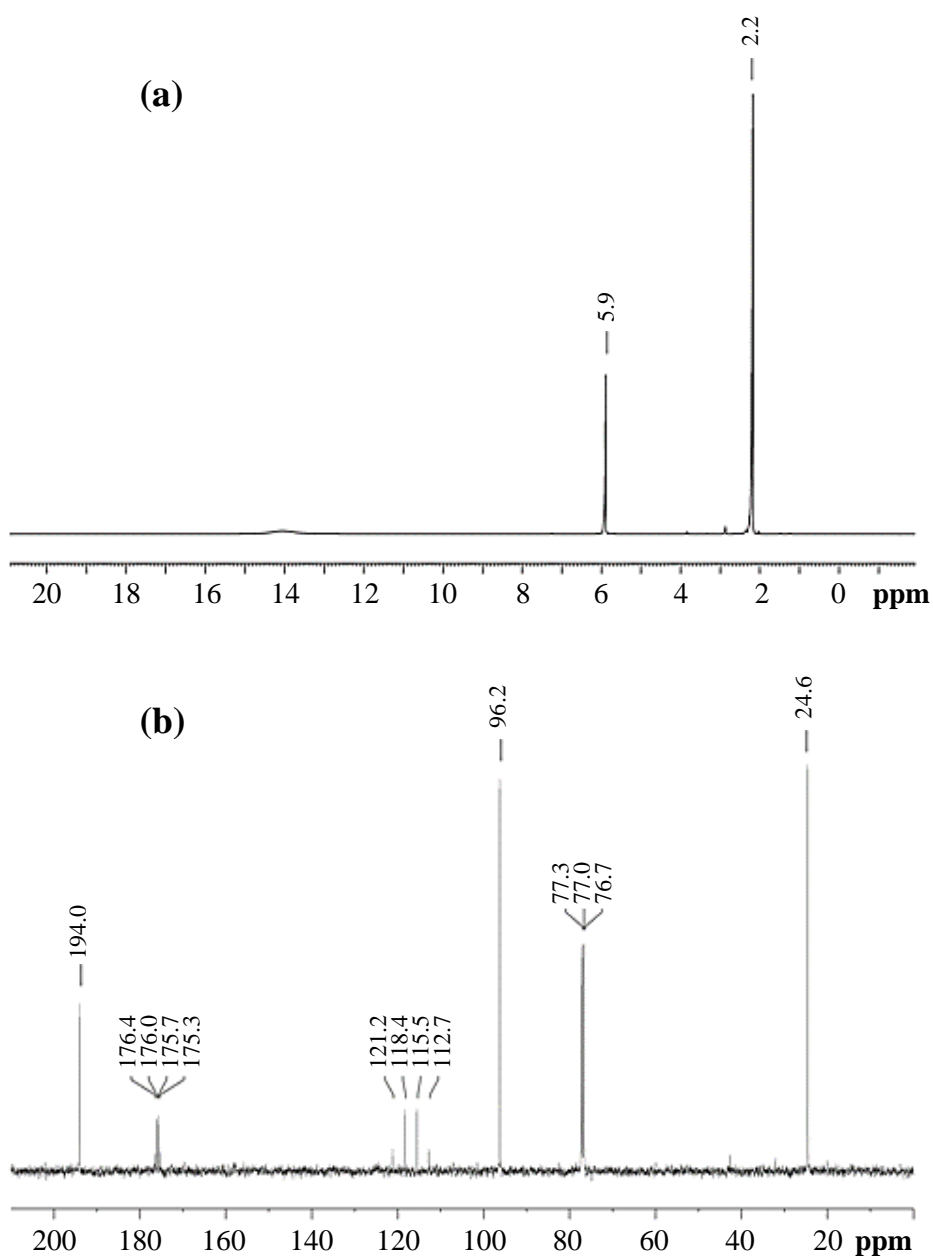
Fig. S9 ^{1}H-NMR (a) and ^{13}C-NMR (b) spectra of Htfa in CDCl₃. In (a), the δ 2.2 ppm represents the methyl, the δ 5.9 ppm the methine proton, and the δ 14 ppm the hydroxyl. The integrals support the assignment. In (b), methyl is at δ 24.6 ppm, the methine at δ 96.2 ppm, the -CF₃ is represented by the quartet in the region 121-112 ppm, and the carbonyls are detectable at 176 ppm and 194 ppm. The identified resonances indicate that in solution the reagent undergoes keto-enolic tautomerism, thus producing the spectrum of the enolic form.
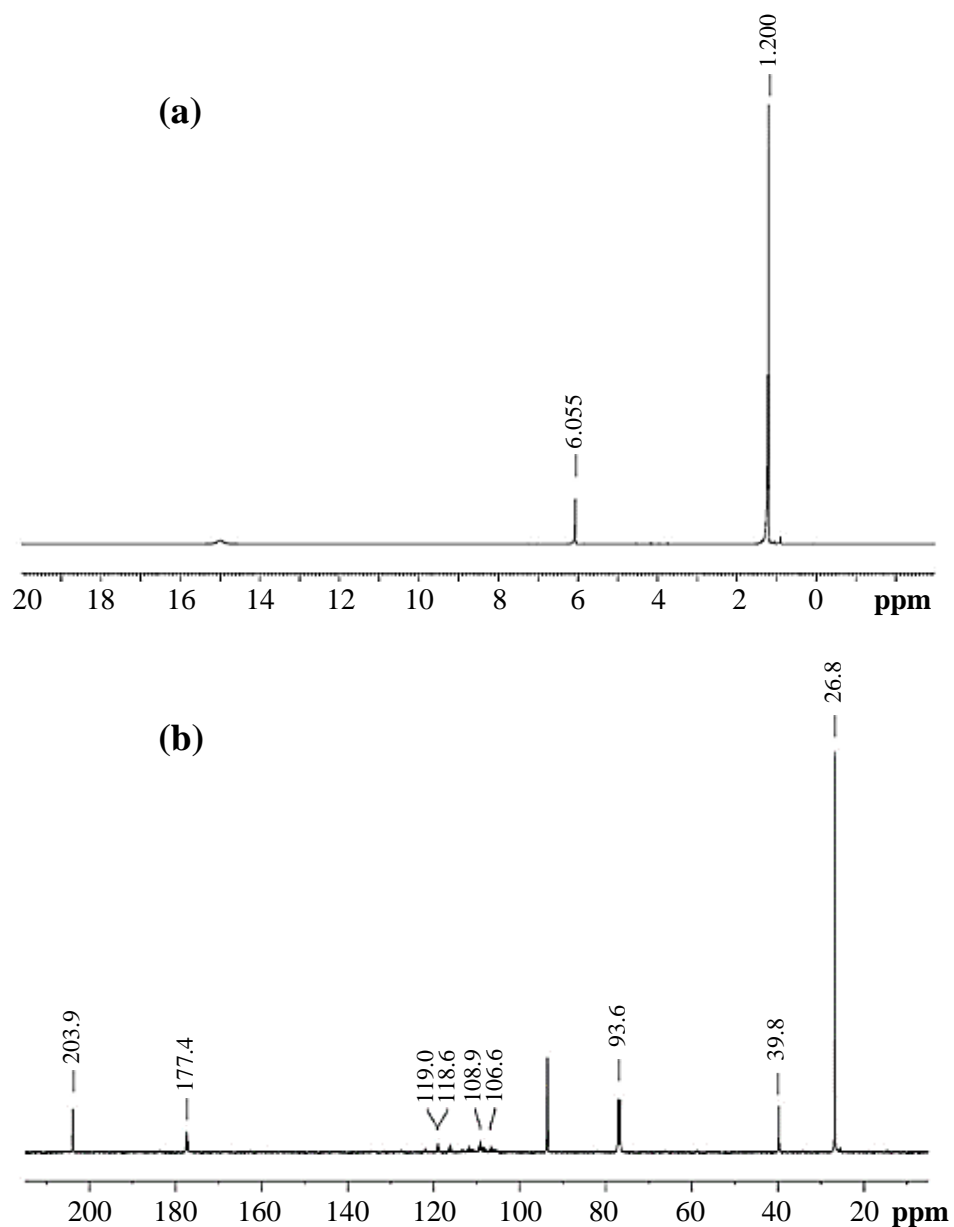
Fig. S10 ^{1}H-NMR (a) and ^{13}C-NMR (b) spectra of Hfod in CDCl$_3$. In (a), the δ 1.2 ppm represents the three methyls, the δ 5.69 ppm the methine proton, and the δ 16.2 ppm the hydroxyl. The integrals support the assignment. In (b), the δ 27 ppm represents the 3 methyls, the δ 39.8 ppm the two quaternary C, the δ 93.6 ppm the methine, and the δ in the region 106-120 ppm the CF signals with their multiplicity due to the large *j*-coupling between C and F. The carbonyls are found at 177.4 ppm and at 201 ppm. The identified resonances indicate that in solution the reagent undergoes keto-enolic tautomerism, thus producing the spectrum of the enolic form.
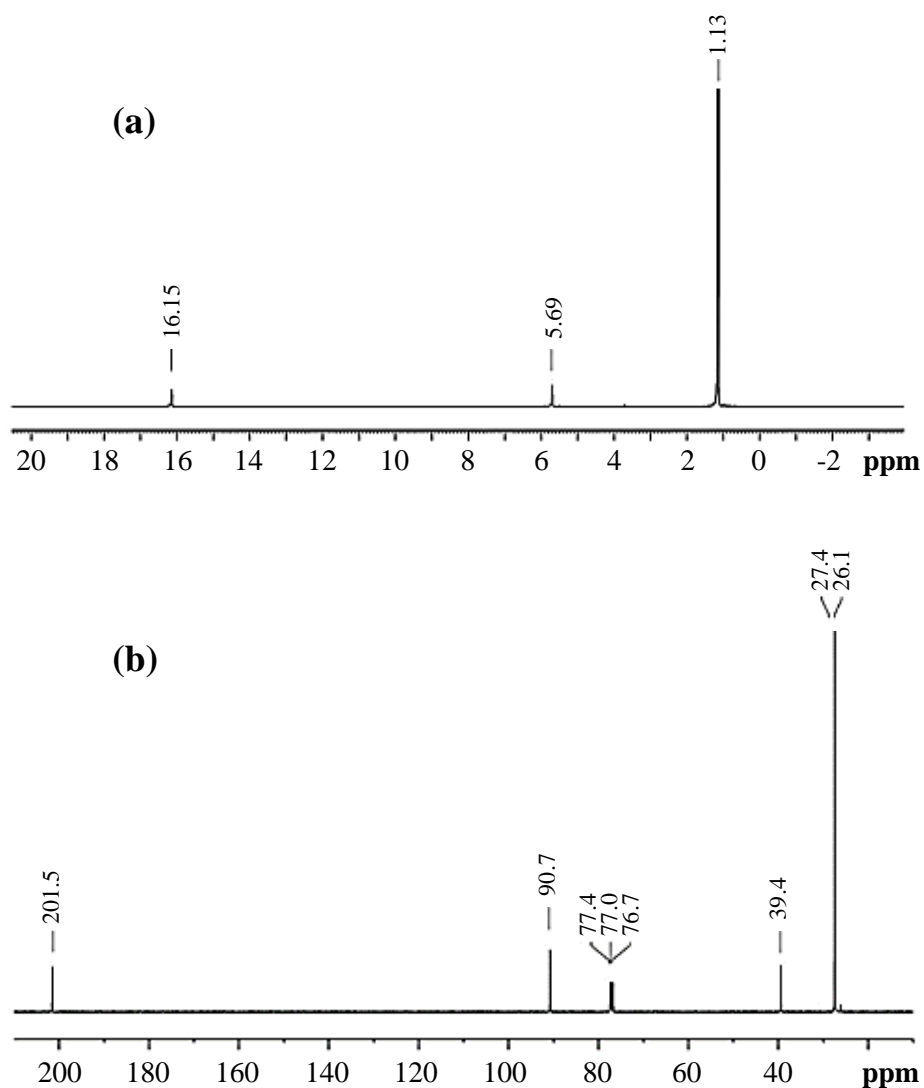
Fig. S11 ^{1}H-NMR (a) and ^{13}C-NMR (b) spectra of Hthd in CDCl$_3$. In (a), the δ 1.1 ppm represents the 18 methyl protons, the δ 5.69 ppm the methine proton, and the δ 16.2 ppm the hydroxyl. The integrals confirm the assignment. In (b), the δ 27 ppm represents the 6 methyls, the δ 39.4 ppm the two quaternary C, and the δ 90.7 ppm the methine; the carbonyls can be detected at δ 201 ppm. The indicated resonances suggest that in solution the reagent undergoes keto-enolic tautomerism, thus producing the spectrum of the enolic form.
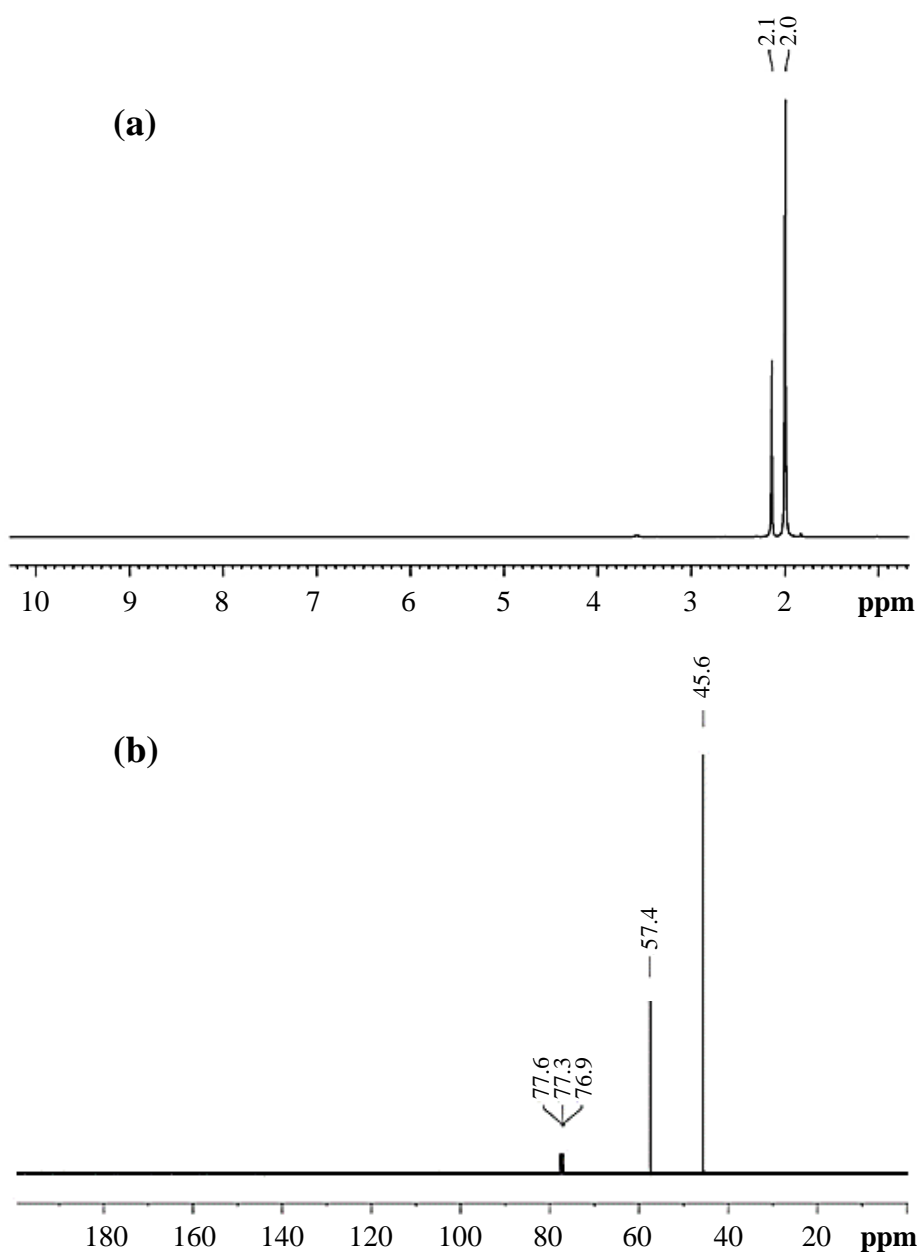
Fig. S12 ^{1}H-NMR (a) and ^{13}C-NMR (b) spectra of TMEDA in CDCl$_3$. In (a), the signals at δ 2.0 ppm and 2.1 ppm can be assigned to methyl and methylene protons, respectively. In (b), the δ 45.6 ppm signals is related to four methyl groups, and the δ 57.4 ppm one is related to the two methylene ones. The integrals confirm the assignment.

§ S6. Electronic transitions

Electronic structure analysis allowed to gain molecular-level information on the optical spectra pertaining to the investigated Ni complexes. The molecular spin orbitals predominantly involved in the electronic excitation components of the most intense band in the optical spectra of **1-3** are shown in Fig. S13. In all cases, the initial and final states of the transition are mainly localized on combinations of the β-diketonate π- and π-* states, respectively, with very scarce contributions from Ni-d states. The initial states of the transition also include a very weak component ascribable to TMEDA states, which is higher in the case of **3** (Fig. S13C). Nonetheless, due to the large predominance of β-diketonate contributions in the involved spin-orbitals, the character of the main band can safely be considered as ligand-ligand π-π* for all the three complexes.
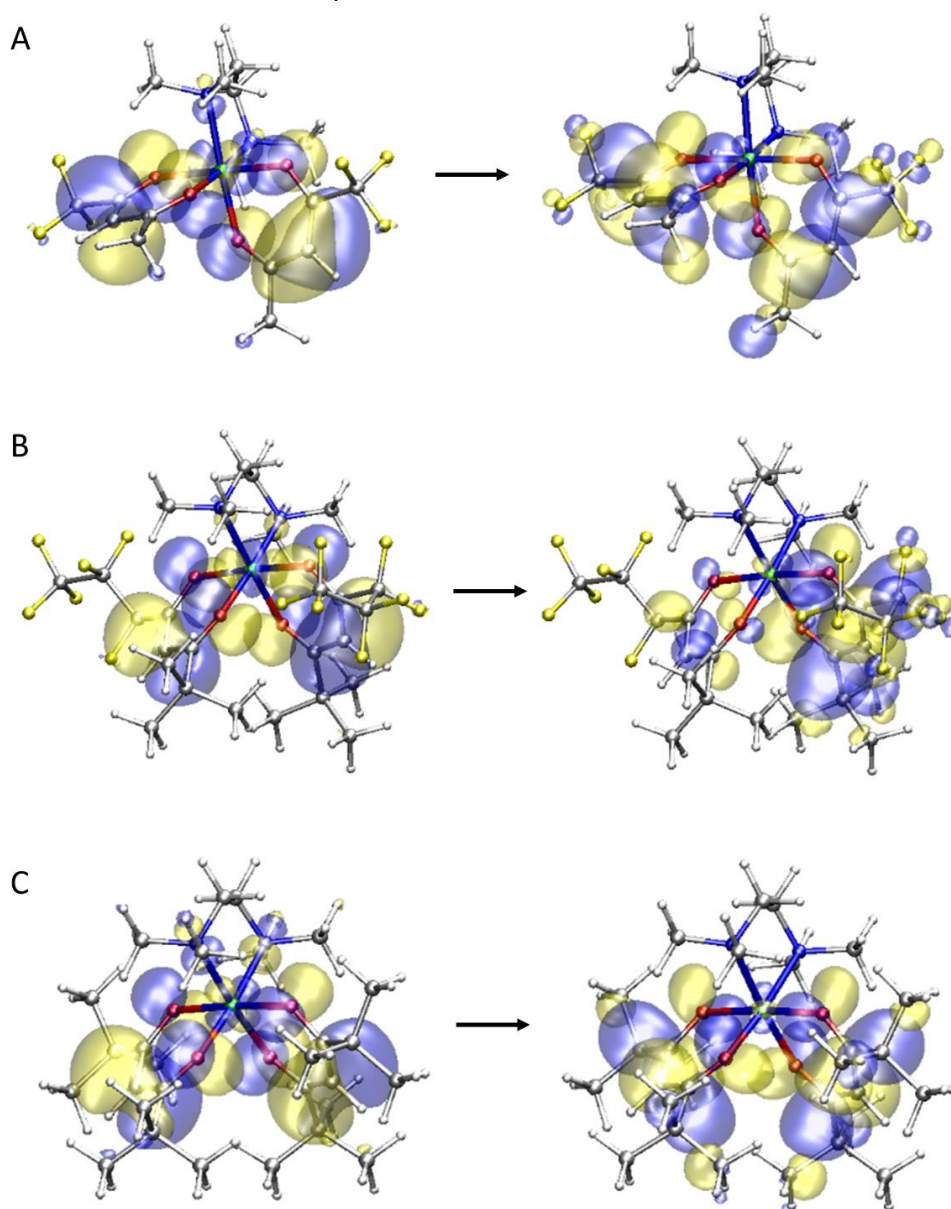
Fig. S13 Graphical representation of the spin orbitals mostly involved in the electronic transition responsible of the main band in the UV-Vis spectra of the investigated Ni-complexes. A: compound **1** (λ = 277 nm); B: compound **2** (λ = 290 nm); C: compound **3** (λ = 271 nm). Yellow and blue colors indicate positive (+0.02 e) and negative (-0.02 e) isosurface values of the spin orbitals, respectively.

§ S7. Thermal analyses
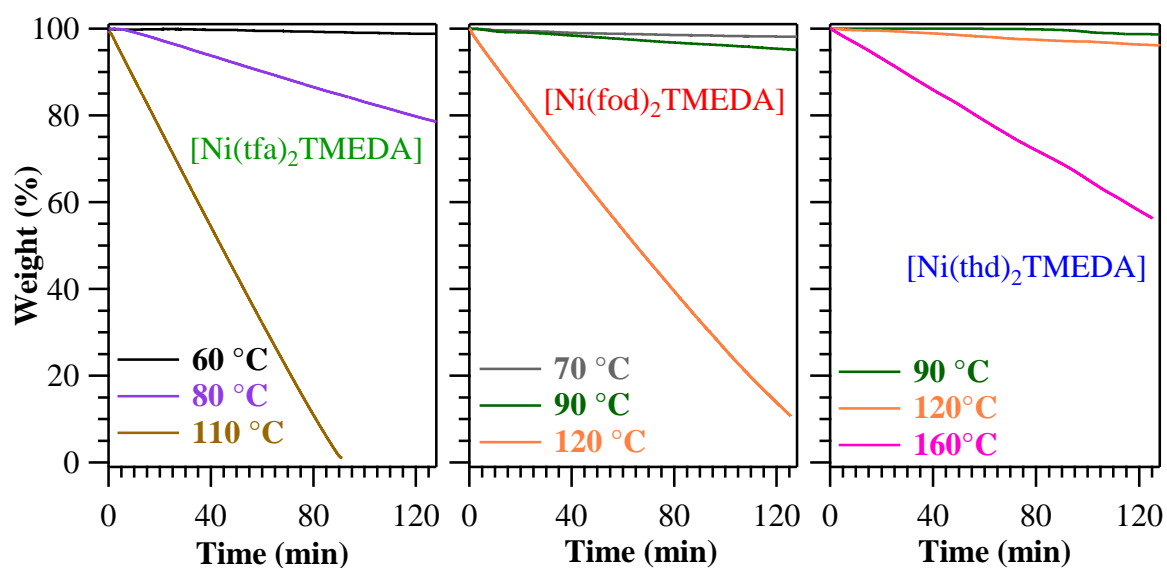
Fig. S14 Isothermal weight losses as a function of time recorded at selected temperatures for compounds [Ni(tfa)$_2$TMEDA] (**1**), [Ni(fod)$_2$TMEDA] (**2**), and [Ni(thd)$_2$TMEDA] (**3**).

Isothermal analyses carried out at selected temperatures were characterized by a linear trend as a function of time, with increasing slopes at higher working temperatures, suggesting the occurrence of a constant vaporization rate as a function of time.[25] Overall, these outcomes, in line with previous results on Mn, Fe, and Co hfa and tfa derivatives,[16, 20, 21, 26-28] underline a long-term thermal stability and a volatilization free from undesired side decompositions. These characteristics are a key prerequisite in view of CVD/ALD end-uses, since they allow a constant and reproducible precursor vapor supply throughout deposition experiments aimed at NiO fabrication.

§ S8. Chemico-physical characterization of NiO thin films

§ S8.1 Experimental

X-ray diffraction (XRD) measurements were carried out by a Bruker AXS D8 Advance Plus diffractometer, equipped with a Göbel mirror and a CuKα X-ray source powered at 40 kV, 40 mA (0.06 °/step; 10 s/step). The analyses were performed at the PanLab facility (Department of Chemical Sciences, Padova University) founded by MIUR Dipartimento di Eccellenza grant "NExuS". For films obtained from **3**, the average crystallite size (*D*) was calculated by the Scherrer formula.[29-34] Dislocation density (*δ*) and microstrain (*ε*) values were estimated as previously reported.[29, 35-38]

Field emission–scanning electron microscopy (FE-SEM) and energy-dispersive X-ray spectroscopy (EDXS) analyses were performed using a Zeiss field emission SUPRA 40 VP apparatus equipped with an INCAx-act PentaFET Precision spectrometer (Oxford Instruments), at primary beam voltages comprised between 10 and 20 kV. The mean nanoaggregate dimensions and deposit thickness values were estimated through a statistical image analysis using the ImageJ® software-

Atomic force microscopy (AFM) characterization was performed in air by a NT-MDT SPM Solver P47H-PRO instrument operated in tapping mode. After plane fitting, root-mean-square (RMS) roughness values were obtained from the height profile of the recorded images.

XPS characterization was performed using a ThermoFisher Scientific ESCALB^{TM} QXi spectrometer, with a monochromatized AlKα source (hν = 1486.6 eV). Binding energy (BE) values were corrected for charging by assigning a position of 284.8 eV to the C1s photopeak of adventitious carbon.[39] Atomic percentages (at.%) were evaluated using sensitivity factors provided by ThermoFisher. Sputtering was carried out by Ar$^+$ bombardment at 3.5 keV for 5 min.

§ S8.2 X-ray diffraction (XRD)
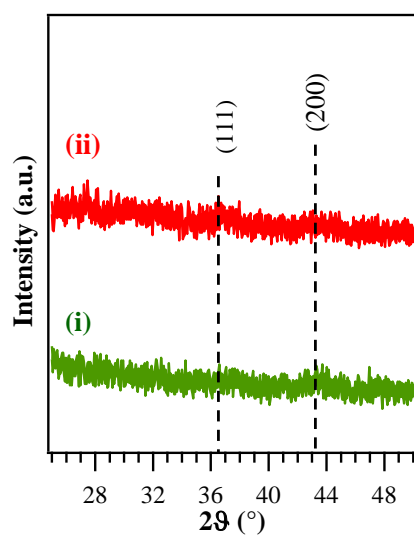
Fig. S15 XRD patterns of specimens deposited on Si(100) from [Ni(tfa)$_2$TMEDA] (i) and [Ni(fod)$_2$TMEDA] (ii). Vertical dashed lines mark reference (111) and (200) peak positions for to cubic NiO.[40]

Precursor	Thickness (nm)	Growth rate (nm×min^{-1})	D (nm)	$I_{(200)}/I_{(111)}$ [a]	δ (lines×m^{-2})	ε
[Ni(tfa)$_2$TMEDA] (1)	(10±1)	0.08	-	-	-	-
[Ni(fod)$_2$TMEDA] (2)	(10±2)	0.08	-	-	-	-
[Ni(thd)$_2$TMEDA] (3)	(37±2)	0.31	(14±1)	1.4	5.1×10^{15}	0.386

Table S7 Processing conditions and relevant material properties for NiO nanodeposits obtained on Si(100) at 400°C under dry O$_2$ atmospheres.

§ S8.3 Atomic force microscopy (AFM) and field emission-scanning electron microscopy (FE-SEM)
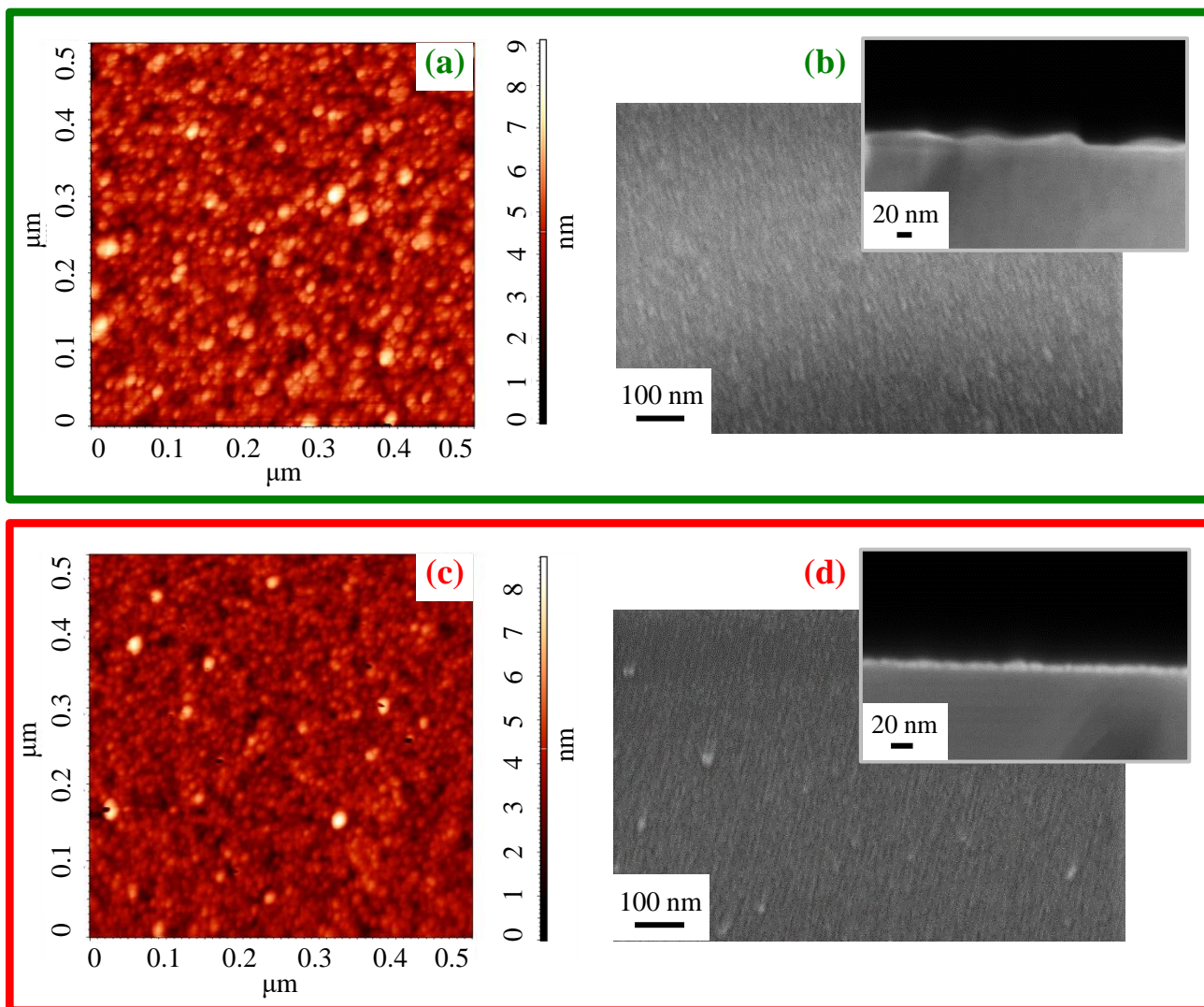
Fig. S16 (from left to right) AFM micrographs, plane-view and cross-sectional FE-SEM images for NiO deposits obtained from [Ni(tfa)$_2$TMEDA] (a-b) and [Ni(fod)$_2$TMEDA] (c-d). The average root-mean-square (RMS) roughness, measured by AFM analyses, was evaluated to be 0.8 nm and 0.6 nm for [Ni(tfa)$_2$TMEDA] and [Ni(fod)$_2$TMEDA], respectively.
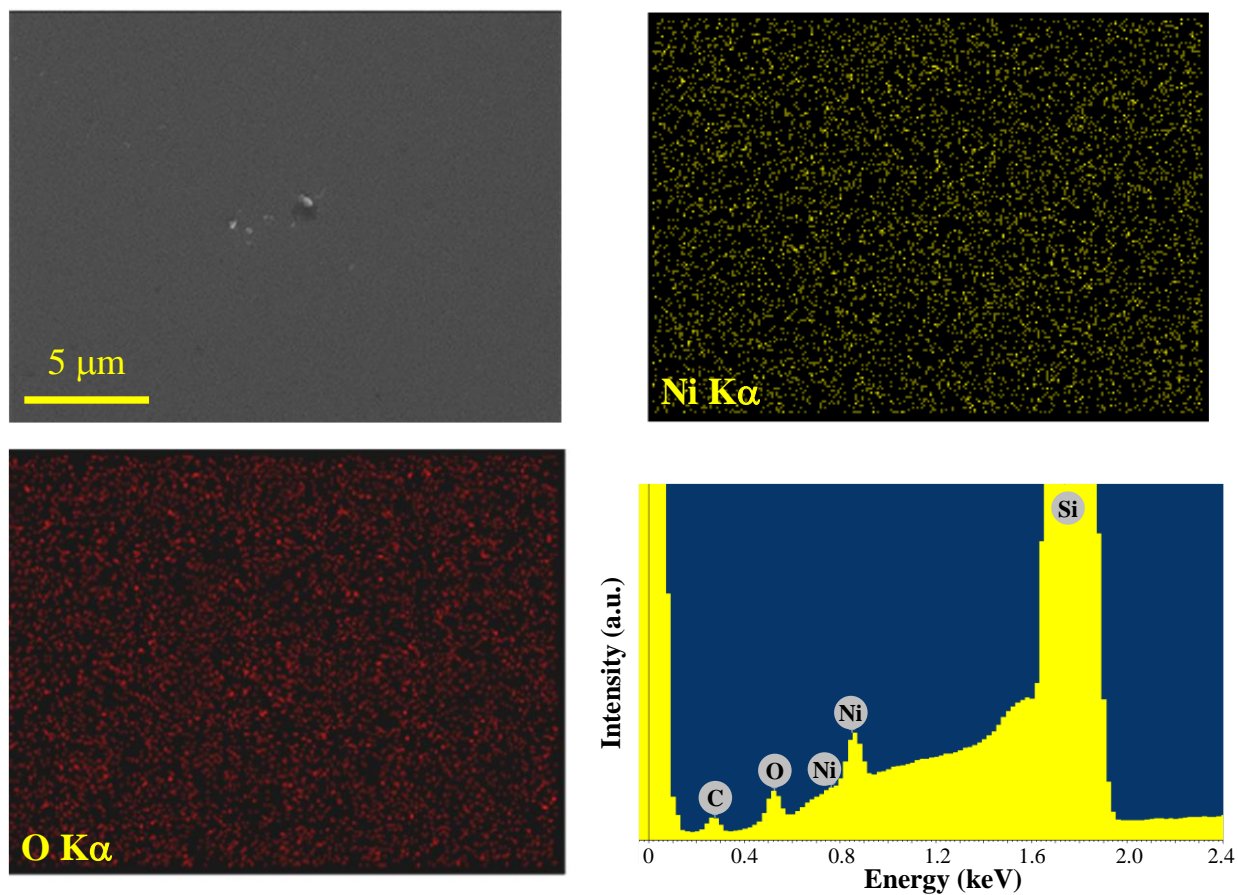
Fig. S17 Ni and O energy dispersive X-ray spectroscopy (EDXS) elemental maps, recorded on the corresponding electron image, for a NiO specimen obtained from [Ni(tfa)$_2$TMEDA], and representative spectrum.
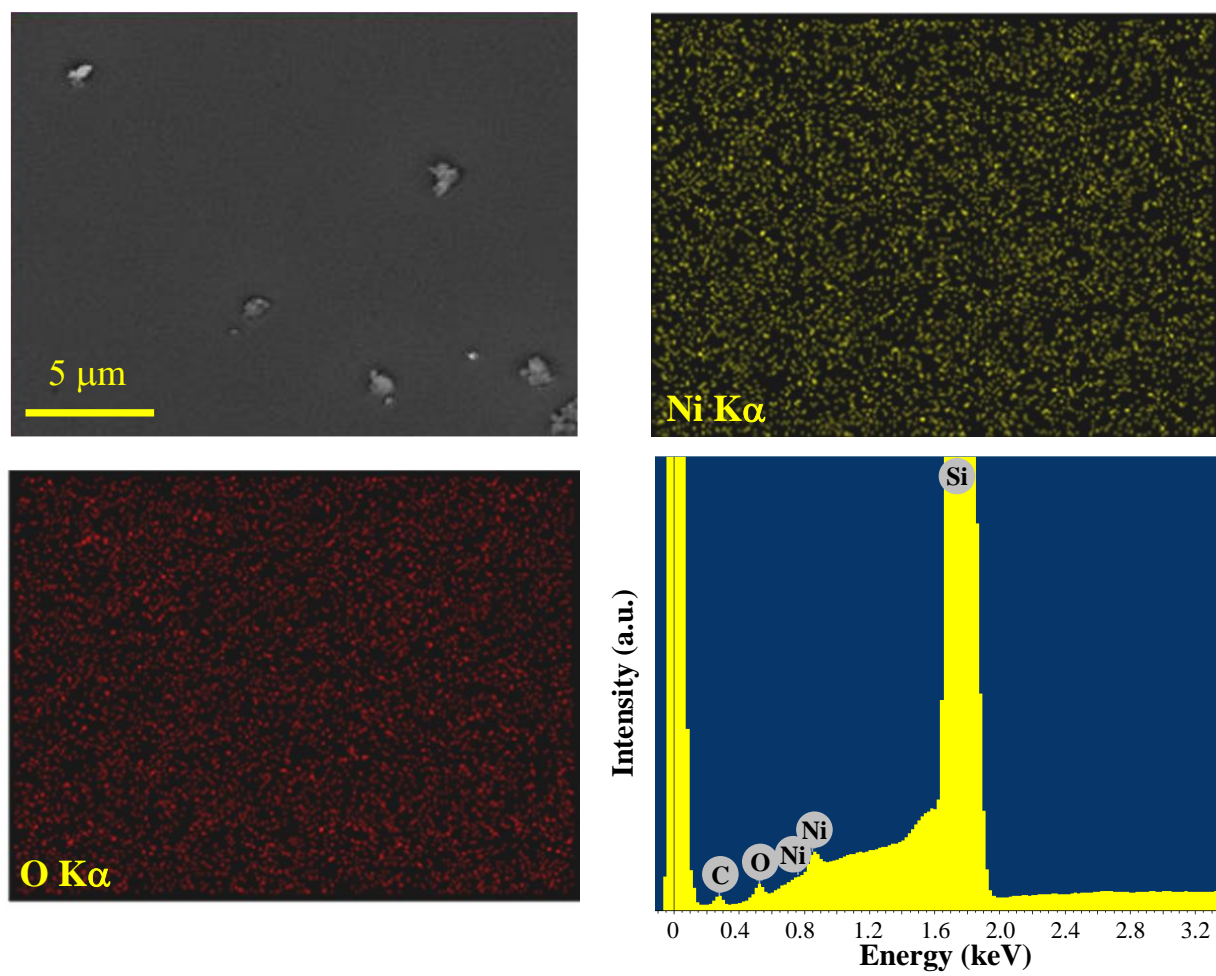
Fig. S18 Ni and O energy dispersive X-ray spectroscopy (EDXS) elemental maps, recorded on the corresponding electron image, for a NiO specimen obtained from [Ni(fod)$_2$TMEDA], and representative spectrum.

§ S8.5 X-ray photoelectron spectroscopy (XPS)
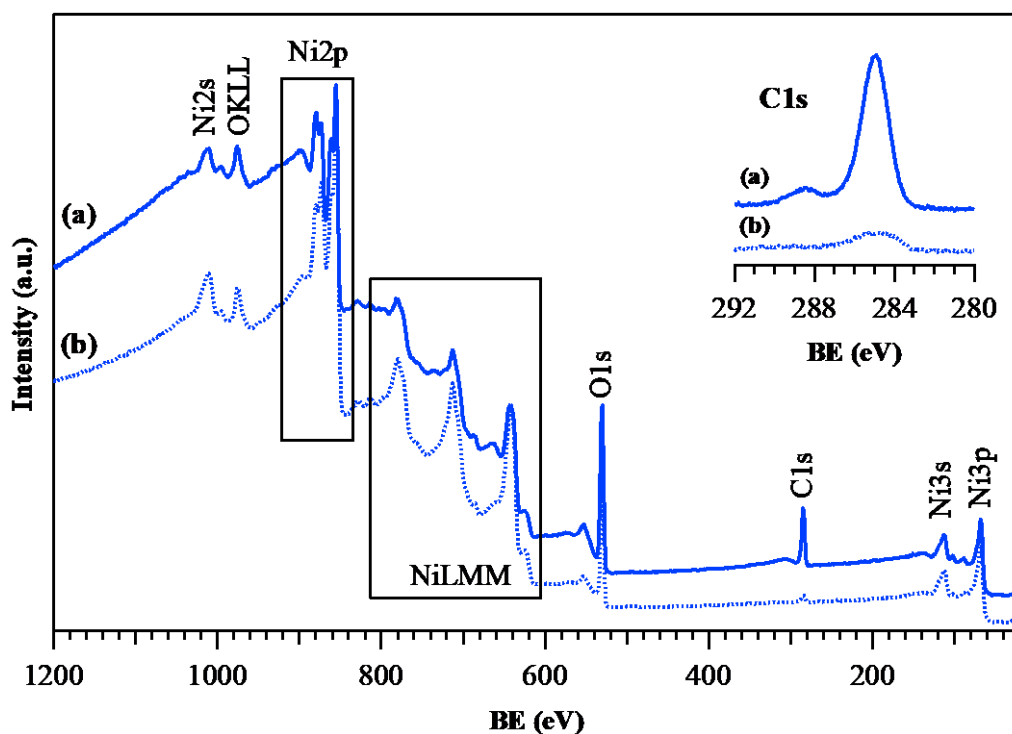
Fig. S19 XPS wide-scan spectra of a NiO sample obtained from [Ni(thd)$_2$TMEDA]: a) surface; b) after Ar$^+$ erosion. Inset: C1s photoelectron peaks in the two cases. Spectra have been vertically shifted for clarity.

Fig. S19 displays survey spectra for a representative sample before and after Ar$^+$ erosion. The surface spectrum was characterized by the presence of carbon, oxygen and nickel, whose content corresponded to 32.5, 40.6 and 26.9, at.% respectively. The Ni2p signal was in agreement with the presence of pure NiO.[41, 42] The surface O/Ni atomic ratio was evaluated to be 1.5, indicating the presence of excess oxygen due to surface hydroxylation/carbonation. The C1s photoelectron peak (Fig. S19, (a) inset) presented a shoulder at higher BEs ($\approx$288.3 eV) with respect to the main adventitious component, attributed to adsorbed carbonates.[41] After Ar$^+$ erosion, the C1s signal underwent an appreciable intensity decrease (Fig. S19, (b) inset); C at.% = 7.0), thus indicating that contamination was mainly confined to the sample surface. Correspondingly, the O/Ni ratio was evaluated to be 1.0, the stoichiometric value expected for nickel(II) oxide. This result, in agreement with XRD analyses, confirmed the presence of NiO in the target system.

§ S9. References

1   *SAINT*, Version 8.40A, Bruker AXS Inc., Madison, Wisconsin, USA, 2016.

2   *SADABS*, Version 2016/2, Bruker AXS Inc., Madison, Wisconsin, USA, 2016.

3   G. M. Sheldrick, *Acta Crystallogr., Sect. A*, 2015, **71**, 3-8.

4   G. M. Sheldrick, *Acta Crystallogr., Sect. C*, 2015, **71**, 3-8.

5   C. B. Hübschle, G. M. Sheldrick and B. Dittrich, *J. Appl. Crystallogr.*, 2011, **44**, 1281-1284.

6   *International Tables for Crystallography, Vol. C* (Ed.: A. J. Wilson), Kluwer Academic Publishers, Dordrecht, The Netherlands, **1992**, Tables 6.1.1.4 (pp. 500–502), 4.2.6.8 (pp. 219–222), and 4.2.4.2 (pp. 193–199).

7   C. F. Macrae, I. Sovago, S. J. Cottrell, P. T. A. Galek, P. McCabe, E. Pidcock, M. Platings, G. P. Shields, J. S. Stevens, M. Towler and P. A. Wood, *J. Appl. Cryst.*, 2020, **53**, 226-235.

8   C. Stienen, J. Grahl, C. Wölper, S. Schulz and G. Bendt, *RSC Adv.*, 2022, **12**, 22974-22983.

9   M. J. Frisch, G. W. Trucks, H. B. Schlegel, G. E. Scuseria, M. A. Robb, J. R. Cheeseman, G. Scalmani, V. Barone, B. Mennucci, G. A. Petersson, H. Nakatsuji, M. Caricato, X. Li, H. P. Hratchian, A. F. Izmaylov, J. Bloino, G. Zheng, J. L. Sonnenberg, M. Hada, M. Ehara, K. Toyota, R. Fukuda, J. Hasegawa, M. Ishida, T. Nakajima, Y. Honda, O. Kitao, H. Nakai, T. Vreven, J. A. Montgomery Jr., J. E. Peralta, F. Ogliaro, M. Bearpark, J. J. Heyd, E. Brothers, K. N. Kudin, V. N. Staroverov, T. Keith, R. Kobayashi, J. Normand, K. Raghavachari, A. Rendell, J. C. Burant, S. S. Iyengar, J. Tomasi, M. Cossi, N. Rega, J. M. Millam, M. Klene, J. E. Knox, J. B. Cross, V. Bakken, C. Adamo, J. Jaramillo, R. Gomperts, R. E. Stratmann, O. Yazyev, A. J. Austin, R. Cammi, C. Pomelli, J. W. Ochterski, R. L. Martin, K. Morokuma, V. G. Zakrzewski, G. A. Voth, P. Salvador, J. J. Dannenberg, S. Dapprich, A. D. Daniels, O. Farkas, J. B. Foresman, J. V. Ortiz, J. Cioslowski and D. J. Fox, *GAUSSIAN 09* (*Revision B.01*), Gaussian, Inc., Wallingford CT, 2009.

10 J.-D. Chai and M. Head-Gordon, *Phys. Chem. Chem. Phys.*, 2008, **10**, 6615-6620.

11 T. H. Dunning, P. J. Hay, in *Modern Theoretical Chemistry*, Chap. 1, Vol. 2, Plenum, New York, 1976.

12 A. Bergner, M. Dolg, W. Küchle, H. Stoll and H. Preuß, *Mol. Phys.*, 1993, **80**, 1431-1441.

13 R. W. Zoellner, C. D. Latham, J. P. Goss, W. G. Golden, R. Jones and P. R. Briddon, *J. Fluorine Chem.*, 2003, **121**, 193-199.

14 G. Bandoli, D. Barreca, A. Gasparotto, R. Seraglia, E. Tondello, A. Devi, R. A. Fischer, M. Winter, E. Fois, A. Gamba and G. Tabacchi, *Phys. Chem. Chem. Phys.*, 2009, **11**, 5998-6007.

15 D. Barreca, G. Carraro, E. Fois, A. Gasparotto, F. Gri, R. Seraglia, M. Wilken, A. Venzo, A. Devi, G. Tabacchi and C. Maccato, *J. Phys. Chem. C*, 2018, **122**, 1367-1375.

16 D. Barreca, G. Carraro, A. Gasparotto, C. Maccato, R. Seraglia and G. Tabacchi, *Inorg. Chim. Acta*, 2012, **380**, 161-166.

17 G. Tabacchi, E. Fois, D. Barreca and A. Gasparotto, *Phys. Status Solidi A*, 2014, **211**, 251-259.

18 https://cccbdb.nist.gov/vibscalejust.asp.

19 D. Johnson III, *NIST Computational Chemistry Comparison and Benchmark Database*, version 21; August 2020, NIST Standard Reference Database N°101.

20 M. Klotzsche, D. Barreca, L. Bigiani, R. Seraglia, A. Gasparotto, L. Vanin, C. Jandl, A. Pöthig, M. Roverso, S. Bogialli, G. Tabacchi, E. Fois, E. Callone, S. Dirè and C. Maccato, *Dalton Trans.*, 2021, **50**, 10374-10385.

21 D. Barreca, L. Bigiani, M. Klotzsche, A. Gasparotto, R. Seraglia, C. Jandl, A. Pöthig, E. Fois, L. Vanin, G. Tabacchi, M. Roverso, S. Bogialli, E. Callone, S. Dirè and C. Maccato, *Mater. Chem. Phys.*, 2022, **277**, 125534.

22 J. D. Epperson, L.-J. Ming, B. D. Woosley, G. R. Baker and G. R. Newkome, *Inorg. Chem.*, 1999, **38**, 4498-4502.

23 A. J. Vila, B. E. Ramirez, A. J. Di Bilio, T. J. Mizoguchi, J. H. Richards and H. B. Gray, *Inorg. Chem.*, 1997, **36**, 4567-4570.

24 M. Kruck, D. C. Sauer, M. Enders, H. Wadepohl and L. H. Gade, *Dalton Trans.*, 2011, **40**, 10406-10415.

25 M. Chandrakala, S. Raj Bharath, T. Maiyalagan and S. Arockiasamy, *Mater. Chem. Phys.*, 2017, **201**, 344-353.

26 G. Bandoli, D. Barreca, A. Gasparotto, C. Maccato, R. Seraglia, E. Tondello, A. Devi, R. A. Fischer and M. Winter, *Inorg. Chem.*, 2009, **48**, 82-89.

27 D. Barreca, G. Carraro, A. Devi, E. Fois, A. Gasparotto, R. Seraglia, C. Maccato, C. Sada, G. Tabacchi, E. Tondello, A. Venzo and M. Winter, *Dalton Trans.*, 2012, **41**, 149-155.

28 C. Maccato, L. Bigiani, G. Carraro, A. Gasparotto, R. Seraglia, J. Kim, A. Devi, G. Tabacchi, E. Fois, G. Pace, V. Di Noto and D. Barreca, *Chem. Eur. J.*, 2017, **23**, 17954-17963.

29 L. Bigiani, D. Barreca, A. Gasparotto, C. Sada, S. Martí-Sanchez, J. Arbiol and C. Maccato, *CrystEngComm*, 2018, **20**, 3016-3024.

30 H. Wang, G. Wu, X. P. Cai, Y. Zhao, Z. F. Shi, J. Wang, X. C. Xia, X. Dong, B. L. Zhang, Y. Ma and G. T. Du, *Vacuum*, 2012, **86**, 2044-2047.

31 H. Wang, Y. Zhao, X. Li, C. Wu, X. Dong, Y. Ma, B. Zhang and G. Du, *Vacuum*, 2015, **119**, 77-80.

32 A. A. Ahmed, M. Devarajan and N. Afzal, *Mater. Sci. Semicond. Process.*, 2017, **63**, 137-141.

33 R. S. Kate, S. C. Bulakhe and R. J. Deokate, *Opt. Quantum Electron.*, 2019, **51**, 319.

34 A. A. Ahmed, N. Afzal, M. Devarajan and S. Subramani, *Mater. Res. Express*, 2016, **3**, 116405.

35 P. Salunkhe, M. A. A V and D. Kekuda, *Mater. Res. Express*, 2020, **7**, 016427.

36 S. Elmassi, A. Narjis, L. Nkhaili, A. Elkissani, L. Amiri, S. Drissi, A. Abali, M. Bousseta and A. Outzourhit, *Physica B*, 2022, **639**, 413980.

37 F. Hajakbari, *J. Nanostruct. Chem.*, 2020, **10**, 97-103.

38 M. S. Jamal, S. A. Shahahmadi, P. Chelvanathan, H. F. Alharbi, M. R. Karim, M. Ahmad Dar, M. Luqman, N. H. Alharthi, Y. S. Al-Harthi, M. Aminuzzaman, N. Asim, K. Sopian, S. K. Tiong, N. Amin and M. Akhtaruzzaman, *Results Phys.*, 2019, **14**, 102360.

39 D. Briggs and M. P. Seah, *Practical surface analysis: Auger and X-ray photoelectron spectroscopy*, John Wiley & Sons: New York, 2nd ed., 1990.

40 Pattern no. 00-0047-1049, JCPDS (2000).

41 J. F. Moulder, W. F. Stickle, P. E. Sobol and K. D. Bomben, *Handbook of X-ray photoelectron spectroscopy*, Perkin Elmer Corporation, Eden Prairie, MN, USA, 1992.

42 https://srdata.nist.gov/xps/.